Author Manuscript

Author Manuscript

Author Manuscript

Author Manuscript

HHS Public Access

Author manuscript

Aerosol Sci Technol. Author manuscript; available in PMC 2015 December 11.

Published in final edited form as:

Aerosol Sci Technol. 2012 ; 46(3): 316–332. doi:10.1080/02786826.2011.625059.

New Approach for Near-Real-Time Measurement of Elemental Composition of Aerosol Using Laser-Induced Breakdown Spectroscopy

Prasoon Diwakar, **Pramod Kulkarni**, and **M. Eileen Birch**

Centers for Disease Control and Prevention, National Institute for Occupational Safety and Health, Cincinnati, Ohio, USA

Abstract

A new approach has been developed for making near-real-time measurement of elemental composition of aerosols using plasma spectroscopy. The method allows preconcentration of miniscule particle mass (pg to ng) directly from the sampled aerosol stream through electrostatic deposition of charged particles (30–900 nm) onto a flat-tip microneedle electrode. The collected material is subsequently ablated from the electrode and monitored by laser-induced breakdown spectroscopy. Atomic emission spectra were collected using a broadband spectrometer with a wavelength range of 200–980 nm. A single-sensor delay time of 1.3 μs was used in the spectrometer for all elements to allow simultaneous measurement of multiple elements. The system was calibrated for various elements including Cd, Cr, Cu, Mn, Na, and Ti. The absolute mass detection limits for these elements were experimentally determined and found to be in the range of 0.018–5 ng. The electrostatic collection technique has many advantages over other substrate-based methods involving aerosol collection on a filter or its focused deposition using an aerodynamic lens. Because the particle mass is collected over a very small area that is smaller than the spatial extent of the laser-induced plasma, the entire mass is available for analysis. This considerably improves reliability of the calibration and enhances measurement accuracy and precision. Further, the aerosol collection technique involves very low pressure drop, thereby allowing higher sample flow rates with much smaller pumps—a desirable feature for portable instrumentation. Higher flow rates also make it feasible to measure trace element concentrations at part per trillion levels. Detection limits in the range of 18–670 ng m^{-3} can be achieved for most of the elements studied at a flow rate of 1.5 L min^{-1} with sampling times of 5 min.

1. Introduction

Exposure to toxic metals and their compounds can cause adverse health effects such as increased risk of cancer and respiratory diseases (Pope et al. 2002; Agency for Toxic Substance and Disease Registry (ATSDR) 2011). Measurement of chemical composition of airborne particulate matter is of great significance to the protection of human health and the environment. Most existing methods for measurement of particulate metal contaminants involve filter-based collection over several hours, followed by laboratory analysis of

Address correspondence to Pramod Kulkarni, Centers for Disease Control and Prevention, National Institute for Occupational Safety and Health, 4676 Columbia Parkway, MS R7, Cincinnati, OH 45226, USA. PSKulkarni@cdc.gov.

Author Manuscript Author Manuscript Author Manuscript Author Manuscript

collected particulate matter using suitable analytical methods. These methods are adequate for routine monitoring applications targeting specific regulations. However, many research applications require measurements below established exposure limits, or demand short measurement times. In addition, even with respect to routine compliance monitoring, the filter-based methods suffer from many known drawbacks. The measurements are time averaged over several hours and cannot capture high-intensity, short-time exposures that are typical in many industrial environments. Filter-based methods are also very time- and resource-intensive, with typical analysis turnaround times of several days to weeks. Semicontinuous or near-real-time instruments that can provide *in situ* information on the chemical composition of aerosols can be valuable tools for monitoring indoor, industrial, and ambient atmospheres. Particularly for workplace or indoor aerosol measurement applications, compact size and portability of the instrument are key to obtaining reliable exposure measurements.

Compared to mass spectrometric methods (Wexler and Murray 2011), plasma-based optical spectroscopy techniques provide a more attractive alternative for measurement of the elemental composition of aerosols. Though single-particle mass spectrometers typically provide the most detailed, real-time information about the size and composition (atomic/molecular) of aerosol particles (Canagaratna et al. 2007; Zelenyuk and Imre 2009; Hao et al. 2009; Wexler and Murray 2011), they are unsuitable for routine exposure measurement applications as they are large, bulky, and expensive. Techniques like laser-induced breakdown spectroscopy (LIBS) are being increasingly applied to field applications due to their relative simplicity and robustness. Rapid progress in laser and optical spectrometer technology has now made it possible to build compact, portable instruments, making LIBS an attractive option for routine field applications where elemental composition is desired (Myers et al. 2003; Gornushkin et al. 2004; Salle et al. 2005; Goujon et al. 2008; Cunat et al. 2009; Leone et al. 2007).

LIBS involves creating a plasma in air, liquid, or on a solid substrate using a high-energy pulsed laser, resulting in atomic emission from the analyte(s), and subsequent detection of emission by an optical spectrometer. Temperatures in the resulting plasma can range from 10,000 to 20,000 K, which vaporizes and atomizes the sample to produce atoms and ions. Each element has signature emission lines, which are collected by appropriate optics and dispersed, typically by using an optical spectrometer, and then, measured with an appropriate detector, such as charge-coupled device (CCD), intensified CCD (ICCD), or a photomultiplier tube (PMT). The wavelength of the atomic emission gives information about the element's identity, while the signal intensity gives its abundance. The LIBS signals are temporal in nature and last for about 10–100 μs after the plasma is formed. The technique has been used for liquids, gases, and solids, including limited application to aerosols (Hahn et al. 1997; Buckley et al. 2000; Fisher et al. 2001), ambient pollution monitoring (Casini et al. 1991; Gaudiuso et al. 2010), industrial process monitoring (Noll et al. 2001, 2008; Fink et al. 2002; Balzer et al. 2006), and standoff or remote detection (Ball et al. 2005; Alvarez-Trujillo et al. 2008; Gottfried et al. 2008).

LIBS has been applied to aerosol analysis with a limited degree of success, particularly with respect to applications where measurements are needed with acceptable precision and

Author Manuscript Author Manuscript Author Manuscript Author Manuscript

accuracy. There are challenges in successfully applying LIBS to aerosols. Because LIBS is a point-based sampling technique, the extremely small sampling volume (typically less than 1 mm^3) results in poor sampling statistics (Hahn et al. 1997), particularly for atmospheric or workplace aerosols. Other key challenges include accuracy, precision, and reliable calibration. Matrix effects, i.e., artifacts introduced by the presence of elements other than the analyte, can also degrade the accuracy of LIBS measurements. Further, the repeatability or precision of aerosol measurement typically has been poor (Cheng 2003; Lithgow et al. 2004; Amodeo et al. 2009). Reliable calibration of aerosol LIBS systems is another key factor that has not been sufficiently addressed by the previous studies. Calibration for measurement of analytes in solution can be reliably performed using certified standard solutions that are stable and have known analyte concentrations, whereas no such standards exist for calibration of aerosol systems. This further necessitates accurate and detailed characterization of aerosol particle properties and wall losses to allow reliable estimation of analyte mass delivered to the plasma volume during the calibration process, which can often be challenging.

Most LIBS studies of aerosol systems fall into two categories: (i) free-stream analysis (FSA) where particles are sampled *in situ* from a free flowing stream and (ii) accumulation of particles from an aerosol stream onto a substrate (such as a filter) followed by LIBS analysis. In the first approach, either particles are randomly sampled at a fixed location in an aerosol stream (Hahn et al. 1997; Buckley et al. 2000; Carranza et al. 2001; Fisher et al. 2001) or they are aligned to form a particle beam, either using a capillary (Cheng 2003; Park et al. 2009) or an aerodynamic lens (Park et al. 2009), which then passes through the laser-induced plasma.

Mass detection limits as low as 0.5 fg (for calcium) have been reported (Carranza et al. 2001; FSA) using high pulse energy (375 mJ) and highly sensitive ICCDs. However, the detection limit in terms of air concentration still tends to be very poor for FSA techniques due to poor sampling statistics. Thus, FSA may not be suitable for analysis of ambient and workplace aerosols at low concentrations. The second approach involving substrate-based collection (SBC) and analysis, though it does not provide as instantaneous information as FSA, does allow one to achieve lower detection limits by increasing the sample flow rates and sampling times. These techniques typically have utilized SBC or collection on a solid substrate using focused aerodynamic impaction (single-particle beam [SPB] analysis) (Cremers and Radziemski 1995; Panne et al. 2001, 2002; Kuhlen et al. 2008; Park et al. 2009). Filter-based collection significantly improves sampling statistics compared to the FSA technique, but likely not enough to be practically useful because only a microscopic point on the filter surface is analyzed each time. For instance, for a 35 mm filter, the amount of sample analyzed in each laser pulse is less than 0.05% of the total collected mass on the filter. To improve sampling statistics, high sampling flow rates, long sample collection times, and/or sampling multiple points on the filter are generally needed. High flow rates in a filter-based system are often not desirable in a compact instrument as it requires larger pumps. Furthermore, the large heterogeneity of deposited particles across the filter surface and along its depth can add to substantial degradation of accuracy and precision of filter-based measurements. SBC using an aerodynamic lens (Park et al. 2009) addresses many of

Author Manuscript Author Manuscript Author Manuscript Author Manuscript

these drawbacks; however, this approach requires multiple, large vacuum pumps and there is a limitation on the particle size range that can be transmitted through the aerodynamic lens, making it unsuitable for compact and portable instrumentation.

In this paper, we present a new approach for sampling and analyzing aerosols using LIBS that addresses many of the drawbacks discussed above. The approach involves first charging and subsequently collecting the charged particles on the flat tip of a microneedle, followed by LIBS analysis of the sample collected on the tip. This allows focused collection of particles on the tip of the needle electrode. The diameter of the collection needle electrode is kept smaller than the spatial extent of the laser-induced plasma, which ensures near-complete ablation of the sample by a single laser pulse. Focused aerosol collection, followed by complete ablation of the deposited material, allows reliable calibration of the system and considerably improves overall measurement accuracy and precision. We show that excellent limits of detection can be achieved using modest sampling flow rates and collection times to allow time resolutions of a few seconds to a few minutes for most elements. The experimental setup, calibration process, determination of limits of detection for various elements, and comparison with previously published studies are presented.

2. Experimental Methods

The complete experimental setup used in this study consists of three subsystems: (i) aerosol generation, (ii) aerosol collection, and (iii) the LIBS system. A schematic diagram of the complete setup is shown in Figure 1.

2.1. Aerosol Generation

For calibration experiments, test aerosols were generated using a pneumatic atomizer (model 3076, TSI Inc., Shoreview, MN, USA) to atomize elemental standard solutions. Except for Na, elemental standard solutions with varying elemental concentrations were obtained from Spex Certiprep (Metuchen, NJ, USA) and Inorganic Ventures (Christiansburg, VA, USA). To obtain an Na standard solution, 99.9% pure NaCl salt was dissolved in ultrafiltered DI water (Fisher Scientific, Pittsburgh, PA, USA). The aerosolized elemental standards were subsequently passed through two sequential diffusion dryers for desolvation. The resulting dry aerosol was passed through a differential mobility analyzer (DMA; model 3080, TSI Inc., Shoreview, MN, USA) to obtain a near-monodisperse test aerosol (with geometric standard deviation less than about 1.1) in the size range 30–500 nm. The aerosol from the DMA was then passed through a neutralizer (a Po^{210} source) and an electrostatic precipitator to remove all electrically charged particles. The resulting uncharged and near-monodisperse test aerosol was sent to the aerosol collection system for analysis using LIBS. Typical number concentration of the test aerosol in the study was in the range of 300–7000 particles/cm^3. Table 1 shows the list of elemental standards used for various elements including Cd, Cu, Cr, Mn, and Ti. These stock standards were diluted using ultrafiltered DI water to obtain the desired solution concentration of the analyte, ranging from 100 to 1000 μgmL^{-1}. A constant flow rate of 1.5 L min^{-1} was maintained through the aerosol collection system and was driven by the native pump in the condensation particle counter (CPC; model 3022A, TSI Inc., Shoreview, MN, USA).

Author Manuscript Author Manuscript Author Manuscript Author Manuscript

2.2. Aerosol Collection System

Figure 2 shows the schematic diagram of the aerosol collection system. An electrostatic aerosol collection system was designed to collect particles directly from the gas phase onto a flat tip of a 500 μm diameter straight tungsten needle (Metal Cutting, Cedar Grove, NJ, USA). Tungsten was chosen as the substrate material mainly because of its superior electrical and thermal properties. Additionally, the spectral lines from tungsten did not interfere with the measurement of elements of interest in this study. The tungsten needle used in this study had high chemical purity (99.996%), ensuring negligible interference from trace impurities. Particles were charged using the corona generated by another sharp tip needle made of tungsten (200 μm diameter with 5 μm diameter tip), called the corona needle, as shown in Figures 2 and 3. A high positive potential (~5 kV) was applied to the corona needle using a DC power supply (Bertran S-230, Spellman Corp., Hauppauge, NY, USA) and the collection needle was grounded. A constant corona current of 1 μA was maintained between the two needle electrodes, which resulted in a very stable corona over an extended period of operation. Both needles were located coaxially with a distance of 7 mm between the tip of corona needle and the flat surface of the collection needle (Figure 2). The diameter of the collection needle was chosen to be 500 μm to approximately match the spatial extent of the laser focal spot and laser-induced plasma on the tip, as well as to provide large-enough surface for the aerosol deposition. The diameter of the laser spot was measured to be 560 ± 9 μm by ablating a film of ink on a glass slide and measuring the diameter of ablated spot using an optical microscope.

Aerosol particles entered the collection system through a concentric tube around the corona needle. They acquired electrical charge through attachment of unipolar ions created by the corona needle and subsequently migrated to the surface of the collection needle under the influence of the electric field created by the two needles. The aerosol sample flow, 1.5 L min^{-1} in this study, exited the collection system through another concentric tube around the collection needle as shown in Figure 2. Both the needles were electrically isolated along their lengths using glass tubes to avoid contact with any metallic fittings and fixtures. This insulation was also necessary to eliminate any undesirable electrical field that may be generated in the aerosol flow path. Since it was desirable to collect particles only on the flat surface of the collection needle, the needle was covered with a high dielectric strength sleeve [polyether ether ketone (PEEK), 1.58 mm outer diameter, 0.40 mm wall thickness; McMaster-Carr, Princeton, NJ, USA] to avoid deposition on the side walls of the collection needle as shown in Figure 2. The system was optimized for various parameters including voltage across electrodes, corona current, distance between the electrodes, and the sample flow rates. As will be shown later, this arrangement provided very high capture efficiency of aerosol particles. The capture efficiency of the aerosol collection system was characterized in the size range of 30–900 nm using aerosols from a pneumatic atomizer or condensation monodisperse aerosol generator (CMAG; model 3475, TSI Inc., Shoreview, MN, USA) and subsequently size-classified using a DMA. A CPC was used downstream of the aerosol collection unit to measure the concentration of particles exiting the unit. The concentrations of DMA-classified particles with and without the voltage across the corona needle were measured and used to calculate capture efficiency. Measuring the concentration downstream of the aerosol collection unit ensured that all particle losses, except those occurring in the

Author Manuscript Author Manuscript Author Manuscript Author Manuscript

presence of electric field, were accounted for in the capture efficiency measurement. The mass of particles deposited on the collection needle was determined by taking into account number concentration, collection time, particle mobility diameter, the particle's chemical form and corresponding mass density, and aerosol flow rate. Particles were assumed to be spherical for particle mass estimation. The implications of these assumptions on mass estimation will be discussed later.

2.3. LIBS Setup and Operation

The aerosol collection system described above was housed in a six-way chamber made of Delrin and designed to allow aerosol inlet and outlet flow. The chamber was fitted with a fused silica quartz window (PW1-2025 UV; CVI MellesGriot, Rochester, NY, USA) that provided optical access for laser pulse delivery and collection of the LIBS signal (i.e., atomic emission signal resulting from the laser ablation of deposited particulate matter). A summary of the experimental parameters for the LIBS system is given in Table 2.

The LIBS instrument consists of a Q-switched Nd: YAG pulsed laser operating at 532 nm [5 ns full width at half maximum (fwhm), 1 Hz, 20 mJ], which was focused onto the tip of the collection needle (located in the center of the LIBS chamber) to create the plasma using a condensing lens (50 mm diameter) with a focal length of 100 mm. The axis of the laser beam was oriented at 90° to the axis of the collection needle. The resulting plasma on the tip of the needle ablated the particulate sample collected on the tip, followed by emission from atomic species in the plasma. The LIBS signal was collected using backscattered geometry using a pierced mirror and a condensing lens with 75 mm focal length. The signal was then focused and transmitted through a fiberoptic cable connected to a broadband spectrometer (200–980 nm, 0.1 nm resolution, LIBS2500 Plus, Ocean Optics Inc., Dunedin, FL, USA). The Q-switch of the laser was triggered by the spectrometer software (OOILIBS, version 4.5.07, Ocean Optics, Dunedin, FL, USA); the timing of the laser pulse and signal collection was controlled by the spectrometer. The compact broadband spectrometer allowed simultaneous analysis of multiple elements in the wavelength range 200–980 nm.

The LIBS signal is temporal in nature and lasts for approximately 10–100 μs after the inception of the plasma. Initially, continuum emission dominates, which is mainly the result of Bremsstrahlung (free–free) and recombination radiation (free-bound) from the plasma when the free electrons and ions recombine as the plasma cools down (Hutchinson 2002). After the initial bright continuum emission decays, atomic emission by ions, followed by neutral species, and finally, emission by molecules takes place. Early continuum emission can significantly degrade the signal-to-noise (*S/N*) ratio, especially if the analyte is available in trace amounts in the sample, as is the case in the current study. Therefore, proper gating and integration of the signal is essential to selectively choose a window of time where the continuum emissions are low, but the signal from the analyte is still high. In order to detect the LIBS signal in this study, different delay times were tested and a delay time of 1.3 μs was chosen, at which the *S/N* ratio for most of the elements examined in the present study was found to be adequate. Although the spectrometer can be optimized for each element to achieve a maximum *S/N* ratio, only one delay time was used to allow simultaneous multielemental analysis. A default signal integration time of 1 ms was used for all elements.

Author Manuscript Author Manuscript Author Manuscript Author Manuscript

2.4. Calculation of Peak-to-Base Ratio of LIBS Signal

The raw signal intensity was subsequently converted to a peak-to-base ratio (*P/B*), defined as the integrated absolute atomic emission line intensity normalized to the plasma continuum intensity close to the atomic line spectral region (Hahn 1998; Hohreiter and Hahn 2005; Park et al. 2009). Defined this way, the *P/B* ratio represents the *S/N* ratio for a particular element and accounts for any fluctuations arising from the shift in continuum emission intensity. The *P/B* ratio was calculated from the collected raw spectra of Cu, Cd, Na, and Ti. For Cr and Mn, a Gaussian curve was fitted to the raw spectral data to resolve their peaks and allow subsequent calculation of *P/B* ratio. Gaussian fitting for Cr and Mn was necessary to resolve the analyte peak of interest from overlapping peaks for the element. A single laser shot (pulse) was sufficient to completely ablate the deposited particulate material for most mass loadings. For higher mass loadings (approximately > 10 ng for Na and >50 ng for Cd), multiple laser shots were fired until no analyte signal was observed. All the shots for which $P/B > 1$ were summed to obtain the final *P/B* ratio for that target element.

For blank measurements (i.e., background measurement from the needle without the presence of any analyte), pure ultra-filtered deionized (DI) water was atomized and the LIBS signal was obtained in the spectral region for each analyte under identical experimental conditions. Blank measurements were taken before and after the introduction of metal aerosols and subsequently processed to obtain *P/B* ratio of the blank. The mean blank reading and its standard deviation were obtained by averaging over nine replicate blank measurements at the spectral region of each target analyte.

2.5. Calibration Experiments

Six different elements were studied in this work: Cd, Cr, Cu, Mn, Na, and Ti. A standard solution for each element (Table 1) was prepared. For each element, atomic emission lines were chosen that corresponded to the maximum signal intensity for that element, with the least interference from tungsten lines (i.e., emission from the substrate). The selected wavelength and energy transition levels for each element are summarized in Table 3.

Aerosol particles were collected for a predetermined amount of time that ranged from a few seconds to a few minutes, depending on aerosol concentration, particle size, and the LIBS signal strength. Subsequently, the laser pulse was fired to generate plasma on the needle tip, followed by collection of emission spectra. The collected spectra were analyzed to obtain a *P/B* ratio as described previously. Blank spectra were collected before and after the calibration experiments for each element. A single laser pulse was sufficient to completely ablate the deposited aerosol for most of the mass loadings. Additionally, the needle tip was cleaned by firing multiple laser shots (3–5) after every measurement to ensure that the clean needle tip was available for the next set of measurements. Calibration experiments were performed by using 50 and 80 nm DMA-classified particles; the total mass deposited on the collection needle was changed by varying the collection time. By varying the aerosol collection time, a wide range of mass depositions, from 1 to 200 ng, was achieved to generate a calibration curve. Calibration for most elements was performed using 5–10 mass

Author Manuscript Author Manuscript Author Manuscript Author Manuscript

loadings. The final calibration curve was obtained by averaging over five independent sets of measurements for each mass loading.

4. Results and Discussions

4.1. Particle Capture Efficiency of Collection Needle

It was desirable that all the particles entering the collection system be captured on the tip of the collection electrode with 100% capture efficiency, ensuring accurate measurement of the air concentration of the analyte. Particle mass collected on the collection needle is given by

$$m_p = Q_f t_c \int_0^{d_{p\max}} \eta(d_p)\left(\frac{\pi}{6} d_p^3 \rho_p\right) n(d_p) dd_p, \quad [1]$$

where $\eta(d_p)$ is the particle size-dependent capture efficiency of particles, ρ_p is the particle material density, Q_f is the aerosol volumetric flow rate, t_c is the time over which particles are collected on the tip, and $n(d_p)$ is the number-weighted size distribution of the aerosol represented by the following lognormal distribution:

$$n(d_p) = \frac{N_t}{\sqrt{2\pi} d_p \ln\sigma_g} \exp\left(-\frac{(\ln d_p - \ln d_{pg})^2}{2(\ln\sigma_g)^2}\right), \quad [2]$$

where N_t is the total particle concentration and d_{pg} is the count mean diameter. Capture efficiency $\eta(d_p)$ is governed by the particle size, electrical charge on the particle, flow rate, and intensity and distribution of the electric field between the electrodes. Specifically, the migration velocity of the particle (v_e) due to the external electric field in the direction perpendicular to the needle axis should be larger than its velocity due to flow (v_f) parallel to the needle axis such that it reaches the collection surface in time less than $t = l/v_f$, where l is the distance between the two electrodes. Following these considerations, the distance between the needles and flow rates was optimized to achieve maximum collection efficiency.

The overall capture efficiency of the collection electrode was experimentally determined by measuring the particle number concentration downstream of the collection unit with (N_{out}^{HV}) and without ($N_{out}^{V=0}$) the high voltage on the corona needle and is given by

$$\eta(d_p) = \frac{N_{out}^{V=0}(d_p) - N_{out}^{HV}(d_p)}{N_{out}^{V=0}(d_p)}. \quad [3]$$

By basing the capture efficiency on the outlet concentration, it was ensured that all the particle losses to regions outside the collection needle tip, in the absence of the electrical field, were accounted for in the capture efficiency term. However, this equation does not account for particle loss to regions outside the tip in the presence of electrical field. This may introduce an error in the estimated mass, the implications of which are discussed later in the section on “system calibration.” Also, it was confirmed that no particles were

Author Manuscript Author Manuscript Author Manuscript Author Manuscript

generated by the corona itself. Experimental capture efficiencies were obtained over the entire size range of 30–900 nm using DMA-classified and CMAG-generated particles and are shown in Figure 4. The collection efficiency was close to 99% over a wide range from 30 to 600 nm and then dropped slightly to 97% for larger particles. This implies that the error introduced in the analyte measurement by the nonideal capture efficiency will be between ∼ 1%–3% in the submicrometer size range.

Our one-step, charge-and-collect system in this study was designed and optimized for the submicrometer size range. The collection efficiency of larger particles, with negligible diffusion, is linearly proportional to the particle diameter; therefore, the electrostatic collection technique can be readily extended to particles larger than 1 μm. A more efficient scheme for collection of small as well as larger particles, e.g., PM2.5, would be to separate charging and collection into a two-stage process by first employing a unipolar charger for efficient electrical charging, followed by subsequent collection on the electrode tip in the presence of electric field in a second unit. In real-world measurement applications, decrease in collection efficiency due to accumulation of a thick particulate layer on the collection electrode can be a source of increased uncertainty in the measured air concentration of an analyte. The thickness of the particulate layer and its electrical resistivity play an important role in determining the degree of reduction in collection efficiency (White 1974; McDonald and Sparks 1980; Flagan and Seinfeld 1988; Young et al. 1988; Kanazawa et al. 1997; Zhuang et al. 2000; Huang and Chen 2003). Typically, for most materials, the thickness must be a few millimeters before an appreciable change in collection efficiency occurs. Huang and Chen (2003) have shown that for cement dust particles of 300 nm diameter, the collection efficiency drops by about 4% when the thickness of the particulate layer on the collection electrode reaches 5 mm. In our collection system, assuming a conservative scenario where the aerosol mass concentration is high at 1 mg/m^3, the sample flow rate is 5 lpm, and particle density is 2 g/cm^3, it will take about 390 min to accumulate a particulate layer of 5 mm thickness over a 0.5-mm-diameter electrode. As discussed later, most applications will require much shorter collection times—on the order of a few seconds to minutes—where reduction in collection efficiency is not likely to be a concern.

4.2. Laser-Needle Orientation Effects

For all the elements and for most mass loadings used in the calibration experiments, one laser pulse was sufficient to achieve complete ablation of deposited material. Figure 5 shows the LIBS signal for Ti from the first and second laser shot, clearly indicating that the Ti signal from the second laser pulse was close to the background.

For very high mass loadings, an additional two to three laser pulses were required for complete ablation of analyte mass. We intentionally used a lower energy laser in this study, much lower than those used in most traditional LIBS studies of aerosols (Arnold and Cremers 1995; Cheng 2000; Park et al. 2009), so as to mimic performance of low-power miniature lasers used in field-portable LIBS instruments. In traditional LIBS studies on aerosols, the laser pulse energy is generally in the range of 100–300 mJ/pulse, whereas in the field-portable instruments it is typically in the range of 25–50 mJ/pulse (Panne et al. 2001; Pierce et al. 2004; Goujon et al. 2008). Examination of the bare tip of the collection

Author Manuscript Author Manuscript Author Manuscript Author Manuscript

needle using scanning electron microscopy before and after a laser pulse showed no visible cratering from the ablation, suggesting that the amount of substrate mass ablated in each event was very small. The same collection needle, which was subjected to many thousands of shots, was used in all our experiments reported in this study. We did not conduct detailed investigation of the needle lifetime in this study. However, in another ongoing study (Diwakar and Kulkarni 2011), where pulsed spark plasma is used, instead of the laser plasma, along with identical electrode setup, we did investigate the electrode durability. Pulsed spark plasma energy in the range of 150– 300 mJ/pulse, much higher than the laser energy of 20 mJ/pulse used in this study, was employed. Repeatability of spark plasma characteristics was tested for up to 120,000 sparks and was found to be excellent even after 120,000 sparks. Laser energy used in this study (20 mJ/pulse) was much lower than that used in the spark system. These results suggest that the needle, when subject to the laser plasma should last several hundreds of thousands of pulses.

As mentioned earlier, the laser was oriented perpendicular to the longitudinal axis of the needle due to ease of implementation and to minimize the energy absorbed by the substrate during ablation as shown in Figure 6. However, this perpendicular orientation may lead to some mass deposited in the “shadow region” (i.e., the needle wall between its tip and the end of the dielectric sheath) not being ablated by the laser as shown in Figure 6. This unablated mass can introduce errors in calibration, if not accounted for.

We further probed the extent of this artifact by quantifying the amount of mass deposited in the shadow region. The first few laser pulses were fired in the “initial” orientation to obtain ablated analyte mass (m_{ai}). Subsequently, the collection needle was rotated about its longitudinal axis in three successive steps, each by 90°, and the spectra were recorded for each orientation to determine the total unablated mass in the shadow region (m_{sh}). Table 4 shows the mass of Cd, Cu, and Mn measured using 50 nm particles for each of the three orientations of the needle, averaged over four replicates. As shown in the table, the amount of mass in the shadow region was approximately 12%–14% of the mass in the initial orientation (m_{ai}). Furthermore, this mass fraction was independent of the aerosol chemical composition.

To account for the shadow region mass fraction, Equation (1) was modified as

$$m_p = Q_f t_c \int_0^{d_{p\,\max}} f_s \eta(d_p) \left(\frac{\pi}{6} d_p^3 \rho_p\right) n(d_p) dd_p,$$

where f_s is the fraction of the total deposited mass not ablated in a single fixed orientation of the collection electrode with respect to the laser. A constant value of 0.12 was used for f_s based on the above measurements. The mass fraction in the shadow region is expected to be independent of particle size, as particles randomly (with respect to spatial position) enter the collection unit. This artifact likely can be eliminated by orienting the laser coaxially with the collection needle; however, this was not verified in this work.

Author Manuscript Author Manuscript Author Manuscript Author Manuscript

4.3. Influence of Particle Size on LIBS Signal

Before establishing the limit of detection for various elements, it was necessary to explore the effect of particle size on the LIBS signal. Figure 7 shows the *P/B* ratio of Na as a function of particle mass over the range 0.15–40 ng at different particle diameters. The Na particle mass was varied through a combination of particle diameters (in the range 40–400 nm) and collection times (15 s to 5 min) to obtain data that spanned the entire mass range. Figure 7 shows that all data points fall on a single curve suggesting that the *P*/*B* ratio is proportional to the particle mass irrespective of the particle size. A power law fit to the data (with an R^2 of 0.98) is shown in Figure 7 that adequately describes the response at low as well high mass loadings.

The data imply that the LIBS response is independent of particle size or the microstructural characteristics of the deposit on the collection needle within the particle size range studied in this work. This means that the signal is proportional to the total particulate mass deposited, irrespective of how finely or coarsely the mass is divided. This ensures that the calibration curves generated using monodisperse particles (described in the next section) are therefore applicable to analysis of any polydisperse aerosol in the submicrometer size range.

4.4. System Calibration

We calibrated the system for various elements; typical LIBS spectra for Cd, Cr, Cu, Mn, Na, and Ti are shown in Figure 8.

For each element, the calibration curve was constructed by plotting the *P/B* ratio as a function of mass deposited on the collection needle tip. Mass was estimated from the number of particles deposited on the tip, collection time, flow rate, and chemical composition. The limit of detection (LOD) was estimated using 3σ criteria defined by the International Union of Pure and Applied Chemistry (IUPAC; Boumans 1994) as

$$\mathrm{LOD}=3\sigma/\mathrm{S}, \quad [4]$$

where σ is the standard deviation of the blank at the spectral region for each element and *S* is the sensitivity given by the slope of the calibration curve. Representative calibration curves for Cr, Cd, Mn, and Ti are shown in Figure 9. As shown in Figure 9, calibration curves in this study were linear over a mass range spanning at least one order of magnitude within the mass loading range studied. For some elements, there could be nonlinear effects at higher mass loadings as were seen for Na in Figure 7.

Following curve-of-growth model and experimental observations, atomic emission intensity first increases linearly with the atomic concentration in the plasma volume and then reaches a plateau due to line-width broadening and self-absorption (Gornushkin et al. 1999; Panne et al. 2001; Meissner et al. 2004). This nonlinear relationship between atomic concentration and LIBS signal intensity is more pronounced for resonance lines such as Na I line used in this study. The effect of line width broadening and self-absorption on linearity of the calibration curve is minimized by using a peak integration approach for quantification of LIBS signal, as has been done in this study. Additionally, in our setup, signal saturation can

Author Manuscript Author Manuscript Author Manuscript Author Manuscript

be readily avoided by decreasing the accumulated mass on the collection needle as needed. In fact, for many real-world measurement applications, it is desirable to have the lowest possible collection time to allow high time resolution measurements. However, when performing simultaneous multielement measurements, it is important to ensure that when using a single-sample collection time, measurement of all the analytes can be performed by using the portion of their respective calibration curve before the onset of self-absorption. For the mass loadings used in this work, the onset of self-absorption was observed only for Na.

The reliability of the calibration procedure used in this work depends on the accuracy and precision of estimation of deposited mass on the tip of the collection needle. As noted earlier, the deposited mass, in the calibration experiments, was calculated based on the following assumptions: (i) spherical particle shape, (ii) mobility diameter, instead of particle's physical size, can be used to calculate mass, and (iii) the particles were devoid of any moisture. Implications of these assumptions, with respect to the error introduced in the calibration, are discussed below.

Departure of particle shape from sphericity, as characterized by dynamic shape factor, can introduce errors using the above approach. Dynamic shape factor (χ), i.e., the ratio of friction or viscous drag on the nonspherical particle to that on the spherical particle of the same volume, is 1 for spherical particles and > 1 for most nonspherical particles. For a nonspherical particle with $\chi > 1$, calculating its mass using its mobility diameter and a spherical shape leads to an overestimation of mass. To probe the extent of this error, we calculated percent mass overestimation at different dynamic shape factors of nonspherical particles and these are listed in Table 5.

These calculations are based on interrelationships between a particle's volume-equivalent and mobility diameters, and its material density and shape factor (Kulkarni et al. 2011). The overestimation of mass can range from approximately 33% at a modest departure from sphericity at $\chi = 1.1$, to a factor of 2.37 at nonspherical shapes with $\chi = 1.5$. NaCl particles have been shown to have dynamic shape factors ranging from 1.02 to 1.24, depending upon the moisture content, drying rate, and the measurement technique used (Wang et al. 2010). Dynamic shape factors for other particles used in this work are not available. Moisture content of the particle can also introduce errors in mass estimation. Particle mass was calculated assuming bulk material density of the salt in its pure chemical form; any presence of moisture in the particle will further lead to overestimation of particle mass (i.e., a specific gravity of the material greater than 1, which was the case for all particles in this study). In our experimental system, we exercised maximum care to desolvate the particles using two successive diffusion dryers and by frequently replenishing the desiccant. However, reduced drying performance, leading to finite moisture content, cannot be completely ruled out, particularly as the desiccant becomes increasingly saturated. This may further contribute toward mass overestimation by a few tens of a percent.

Fluctuation in the number concentration of particles downstream of the DMA during calibration can also introduce uncertainty in mass estimation. The pneumatic atomizer used in this work was a stable source of calibration aerosol with fluctuation in particle number concentration less than 5%.

Author Manuscript Author Manuscript Author Manuscript Author Manuscript

Particle wall loss to regions other than the needle tip, if not accounted for, can also introduce errors in mass estimation. The capture efficiency curves shown in Figure 4 do account for particle loss (mainly deposition due to Brownian diffusion in the size range studied) in the absence of electrical field. However, there can be additional mechanisms of loss of uncharged (due to induced forces from polarization) as well as charged (due to electrophoretic forces) particles in the presence of electrical field. Loss due to polarization of uncharged particles was experimentally confirmed to be negligible in our system. However, loss of charged particles, if any, could lead to error in mass estimation; however, this was not investigated experimentally. Charged particles could deposit in regions other than the collection needle tip due to electrical fields around the collection or corona needle in the aerosol flow path (Figure 2). We used adequate dielectric sheathing around both the needles to concentrate the electrical field on the needle tip to minimize this effect (Figure 2; 0.4 mm PEEK + 1 mm thick glass wall). Our numerical simulations indicate that the electrical field strength falls rapidly with radial distance away from the longitudinal axis of both the needles (Figure 3), suggesting that charged particle loss induced by weak electrical fields in the aerosol flow path is likely to be negligible. Furthermore, the weak electrical fields, if present, can perhaps only capture small particles in the nanometer range (with very small mass) due to their high electrical mobility, thereby introducing only a minor error in mass estimation. Nevertheless, there can be a finite error associated with capture efficiency measurement due to factors mentioned above which can lead to overestimation of mass collected on the needle tip.

Multiple charging of particles in the DMA (Figure 1) can also introduce error in mass estimation. A DMA classifies particles based on their electrical mobility, implying particle size classification only if charge on the particles is known. Particle populations, all of the same electrical mobility but of different physical size and charge levels, can pass through the DMA. This can introduce an artifact when one must classify particles of the same “physical” size. The presence of multiply charged, larger particles in the calibration aerosol can lead to underestimation of particle mass in the calibration process. However, this error can be greatly minimized by ensuring that the classification size in the DMA is larger than the modal diameter of the particle size distribution entering the DMA, as was done in this study. Additionally, an impactor was used prior to the DMA to remove particles larger than 1 μm aerodynamic diameter to minimize interference from larger particles.

Overestimation of particle mass in the calibration procedure also implies overestimation of the LODs, as discussed in the next section. It is worth noting that many sources of errors discussed above are inherent in the calibration of most aerosol spectroscopy systems and therefore are not specific to our system. In fact, the controlled aerosol collection over a very small area on the needle tip in our system enables relatively more accurate and precise delivery of analyte mass to the plasma during the calibration process compared to many other filter-based systems.

4.5. Limits of Detection

Tables 6 and 7 summarize the LODs in terms of absolute mass as well as air concentration for various elements studied in this work. We obtained mass detection limits in the range of

Author Manuscript Author Manuscript Author Manuscript Author Manuscript

0.018–5.03 ng for our system. The collection time ranged from 15 s to 15 min for various mass loadings. The mass accumulated on the electrode tip was a linear function of time over this time period. The reported LOD values are within a factor of 10 of the lowest measured mass in the calibration experiments for most elements (except for Cr), which conforms to conventional practice in spectrochemical analysis (Ingley and Crouch 1988). The LODs in terms of air concentrations in the range of 0.018–0.67 $\mu g\ m^{-3}$ were obtained by using a sample collection time of 5 min and sample flow rate of 1.5 L min^{-1}. Flow rate and collection time can be readily increased, and lower detection limits (in terms of air concentration) can be achieved. Tables 6 and 7 also report LODs for a laboratory inductively coupled plasma-atomic emission spectroscopy (ICP-AES; Spectro Analytical Instruments, Inc., Fitchburg, MA, USA) system. The laboratory ICP-AES instrument was equipped with a monochromator (180–600 nm) and three polychromators for sequential and simultaneous elemental analysis, and used a liquid sample flow rate of 0.001 L min^{-1} with a total sample volume in the ICP plasma of 92.5 μL. As is clearly evident from Tables 6 and 7, detection limits of our system are better than or comparable to that of the ICP-AES system for most elements, except for Cd. As noted earlier, it is possible that LODs of our system are overestimated (i.e., higher than actual) due to assumptions regarding particle shape and moisture content of the particles used in the calibration and due to errors associated with collection efficiency measurements.

LODs reported by other studies on plasma spectroscopy of aerosols are also listed in Tables 6 and 7 for comparison. These studies employed variety of methods that varied widely with respect to plasma source and characteristics, type of detectors, sample flow rates, and sample collection methods. As noted earlier, LIBS studies on aerosols have employed various approaches including FSA, conventional SBC followed by LIBS analysis, and focused collection of SPB on a substrate using an aerodynamic lens for subsequent LIBS analysis. The comparison of LODs in Tables 6 and 7, though complicated by wide differences across different methods, serves to bring out the key qualitative features of various techniques with respect to their sensitivity and suitability for field-portable instrumentation.

LIBS approaches that employ FSA for aerosols typically tend to have low mass detection limits (Carranza et al. 2001; Lithgow et al. 2004) due to better coupling of laser energy and the absence of background emissions from the substrate. As seen in Table 6, using this technique, LODs in the femtogram range can be achieved (Carranza et al. 2001; Lithgow et al. 2004) by employing very sensitive ICCD cameras (which have been shown to increase the *S*/*N* ratio by an order of magnitude; Carranza et al. 2003), gated delay times, and high-energy lasers. However, FSA limits the size of particles that can be spectroscopically detected. For example, an LOD of 3 fg for Ca corresponds to a minimum detectable particle size of 130 nm diameter. The technique also suffers from very poor sampling statistics (which offsets its key advantage of high time resolution requiring averaging over multiple shots) and fixed limit of detection (due to fixed sample flow rate). It is worth noting that the detection limits in terms of air concentration (Table 7) for FSA techniques are in fact much higher than those for our system due to their poor sampling rate.

Author Manuscript Author Manuscript Author Manuscript Author Manuscript

In contrast, substrate-based methods do overcome some of the limitations of FSA techniques, albeit at the cost of higher mass detection limits. Table 6 shows that mass detection limits for a swipe-based LIBS method (Chinni et al. 2010; a bench-top portable unit, aqueous suspensions dried on the swipe followed by LIBS analysis) are 2–5 orders of magnitude higher. Mass detection limits of our system are typically much lower than those for the swipe-based method. Table 7 also shows lower detection limits of our system compared to the filter-based method of Panne et al. (2001, 2002) in spite of lower sampling flow rate and inferior detector in our system. Their system utilized a much higher laser pulse energy (70 mJ/pulse), a higher flow rate (4 L min^{-1}), and longer collection times (1–32 min); an Echelle spectrometer, ICCD, and gated delays (Panne et al. 2001, 2002). Other substrate methods that use focused collection with an aerodynamic lens could perhaps achieve detection limits comparable to our system (Park et al. 2009); however, the method requires use of large vacuum pumps, lower sampling flow rates, and only allows analysis of a limited particle size range. It is also worth noting that the detection limits of our system are an order of magnitude better than those of the microwave-induced plasma spectroscopy system of Duan et al. (2000).

4.6. Precision and Accuracy of Measurements

The precision of LIBS measurements depends on many factors such as laser pulse energy, stability of laser pulse, detector delay, surface roughness of the substrate, sample homogeneity, and number of accumulated spectra (Castle et al. 1998). In addition, as noted earlier, other key sources of uncertainty in the calibration process, such as variation in particle shape/morphology, particle's moisture content, particle size, and number concentration fluctuation, can also be important.

A key source of uncertainty, perhaps ignored by most plasma spectroscopy studies of aerosols, is the ability to deliver a known mass of analyte to the plasma volume during the calibration process. If the mass ablated in each plasma event is known with high accuracy and precision during the calibration process, the overall figures of merit of measurement can be substantially improved. However, as noted earlier, accurately delivering known analyte mass to the plasma volume is challenging in most substrate-based systems. For instance, filter-based methods are calibrated by depositing aerosol of known concentration on the filter surface, followed by discrete LIBS sampling of the filter surface. Therefore, it is highly desirable that the aerosol deposition be spatially homogenous, not only across the filter surface, but also along its depth. This is often not the case in fibrous particulate filters as the deposition generally decreases with depth in the direction of the flow. This heterogeneity can introduce large errors in the calibration process. The needle collection system used in our work largely reduces this uncertainty because the entire mass is concentrated on the needle tip and available for complete ablation. This considerably improves the accuracy and precision of the calibration and hence that of the measurement in a given application.

In this study, five sets of measurements were performed for each element and the relative standard deviation (RSD) of the LIBS signal varied in the range of 1%–21% for all the elements for different mass loadings on the collection electrode tip, except for Cd, which had higher RSD (see Table 8).

Author Manuscript Author Manuscript Author Manuscript Author Manuscript

When the system was operated at higher mass loadings (typically >20 ng), RSDs lower than 10% were observed. The overall repeatability (except for Cd) of our system was better compared to reported values for FSA LIBS techniques that typically have repeatability in the range 25%–42% (Cheng 2003; Lithgow et al. 2004; Amodeo et al. 2009).

The low laser pulse energy used in our system could perhaps lead to the poor repeatability noted above. Higher pulse energies have been shown to give better repeatability due to more stable plasma (Carranza and Hahn 2002). We surmise that using a smaller diameter collection needle and orienting the laser beam coaxially with the collection needle could further lead to reducing uncertainties. Better control of particle morphology and efficient desolvation of aerosols can also substantially reduce the uncertainty of measurements in the calibration process.

We also qualitatively probed the measurement accuracy of the system by measuring the relative concentration of multiple elements in test aerosols of accurately known elemental composition. Stock solutions containing mixtures of elemental standards for Mn, Cr, and Ti were prepared with known ratios. These stock solutions were then used to generate the test aerosol particles. The measured signals from Mn and Cr were then run through calibration curve to obtain the concentrations. The measured concentration ratio thus obtained was then compared against the known concentration ratio in the mixture as shown in Figure 10. The figure shows an excellent agreement, partially confirming the good measurement accuracy of our system.

It should be noted that the presence of other elements in the plasma volume, other than the target analyte, can bias the response, known as “matrix effect” (Diwakar et al. 2007, 2010). Figure 10 shows the absence of significant matrix effects under the experimental conditions used. The good agreement with the measured ratio of elements (Figure 10) also implies that the other sources of errors (not related to matrix effects) affecting the accuracy are likely negligible. A detailed comparison of analyte concentration measurements, and not just the ratios, using an independent analytical method will be necessary to further quantify the measurement accuracy of our system.

4.7. Time Resolution of Measurement

The LODs of various elements obtained in this study are low enough to allow near-real-time measurement of most elements using the technique proposed in this study. The time resolution of measurement for a given application, i.e., the time rate at which the elemental concentration of aerosols is obtained, will depend on many factors such as particle size distribution, concentration of the element of interest, and its LOD. Table 9 shows minimum collection time required for polydisperse aerosols of various inorganic compounds at various geometric mean diameters. The total number concentration (N_t) was assumed to be 100 cm^{-3} and $\sigma_g = 1.5$ was used in the calculations. The minimum collection time t_c was calculated as

Author Manuscript Author Manuscript Author Manuscript Author Manuscript

$$t_c = \frac{LOQ_i}{Q_a \Phi_i \int (\frac{\pi}{6} d_p^3 \rho_i) n(d_p) d d_p}, \quad [5]$$

where, LOQ_i is the limit of quantification, defined as (3.33 × LOD_i), of *i*th element; Q_a is the aerosol sampling flow rate; Φ_i is the fraction of element *i* in the inorganic compound with material density of ρ_i. An aerosol flow rate of 5 L min^{-1} was assumed in the calculations.

As shown in the table, measurement of most aerosols with d_{pg} larger than about 50 nm can be conducted in few seconds to few minutes (except for *Cd*, which had a high detection limit in our system). For particles below 25 nm diameter, collection time on the order of hours may be necessary. It is worth noting that these calculations were performed for very dilute aerosols (with a total number concentration of 100 cm^{-3}). Typically, air concentrations of particles in most industrial and ambient atmospheres are much larger than 100 cm^{-3}. While actual collection times will depend on many factors as noted above and can be substantially different from those shown in Table 9, these estimates are conservative enough to expect the time resolution in most real-world applications to be on the order of few seconds to minutes at moderate flow rates of 1–5 L min^{-1}. These calculations serve to demonstrate the near-real-time capability of our technique.

5. Conclusions

A new approach for collection of airborne particles on a tip of a microneedle has been developed for aerosol chemical analysis using plasma spectroscopy. Our approach allows efficient and focused collection of particles over wide size range on the tip of a microneedle using the electrostatic technique. As a result, accurate and precise delivery of analyte mass to plasma volume can be achieved, thereby allowing reliable calibration. This subsequently improves the overall figures of merit of aerosol measurement compared to other plasma spectroscopy techniques. Also, the electrostatic collection enables use of high sample flow rates with minimal pressure drop, enabling development of compact, field portable instruments. We have demonstrated that for elements studied in this work, detection limits comparable to that of a laboratory ICP-AES system can be achieved with good accuracy and precision. Mass detection limits in the range of 0.018–5 ng could be achieved for the elements studied. This corresponds to limits of detection (in terms of air concentration) in the range of 18–670 ng m^{-3} at a modest 1.5 L min^{-1} sample flow rate and sampling time of 5 min. These limits of detection were far superior compared to earlier LIBS studies on aerosols, particularly considering the high time resolution of our technique. Lower detection limits can be further obtained by increasing the flow rate or the sample collection time. Our system employed low laser pulse energy, a nonintensified detector, and single delay time for all elements to mimic a less complex configuration that is desirable in a field-portable spectrometer. The technique is inherently amenable to miniaturization essential in field-portable instrumentation. The electrode system for aerosol collection can be housed in volume as small as a few cubic centimeters. The technique presents a simple and promising approach that allows development of compact, near-real-time instrumentation employing

Author Manuscript Author Manuscript Author Manuscript Author Manuscript

various spectroscopic techniques, including laser-induced, microwave-induced, or spark-induced plasma spectroscopy, and Raman spectroscopy for aerosol measurements.

Acknowledgments

The authors would like to thank Ronnee Andrews for providing information on the ICP-AES system, and Chaolong Qi and Greg Dye for their help with the experimental work. The findings and conclusions in this report are those of the authors and do not necessarily represent the views of the National Institute for Occupational Safety and Health. Mention of product or company name does not constitute endorsement by the Centers for Disease Control and Prevention.

References

Agency for Toxic Substance and Disease Registry (ATSDR). [accessed on May 27, 2010] Toxicological Profiles. 2011. http://www.atsdr.cdc.gov/toxprofiles/index.asp

Alvarez-Trujillo LA, Ferrero A, Laserna JJ. Preliminary Studies on Stand-Off Laser Induced Breakdown Spectroscopy Detection of Aerosols. J Anal Atom Spectrom. 2008; 23:885–888.

Amodeo T, Dutouquet C, Le Bihan O, Attoui M, Frejafon E. On-Line Determination of Nanometric and Sub-Micrometric Particle Physicochemical Characteristics Using Spectral Imaging-Aided Laser-Induced Breakdown Spectroscopy Coupled with a Scanning Mobility Particle Sizer. Spectrochim Acta B-Atom Spectrosc. 2009; 64:1141–1152.

Amodeo T, Dutouquet C, Tenegal F, Guizard B, Maskrot H, Le Bihan O, Frejafon E. On-Line Monitoring of Composite Nanoparticles Synthesized in a Pre-Industrial Laser Pyrolysis Reactor using Laser-Induced Breakdown Spectroscopy. Spectrochim Acta B-Atom Spectrosc. 2008; 63:1183–1190.

Arnold SD, Cremers DA. Rapid-Determination of Metal Particles on Air Sampling Filters Using Laser-Induced Breakdown Spectroscopy. Am Ind Hyg Assoc J. 1995; 56:1180–1186.

Ball AJ, Hohreiter V, Hahn DW. Hydrogen Leak Detection Using Laser-Induced Breakdown Spectroscopy. Appl Spectrosc. 2005; 59:348–353. [PubMed: 15901317]

Balzer H, Hoehne M, Noll R, Sturm V. New Approach to Online Monitoring of the Al Depth Profile of the Hot-Dip Galvanised Sheet Steel Using LIBS. Anal Bioanal Chem. 2006; 385:225–233. [PubMed: 16570144]

Boumans PWJM. Detection Limits and Spectral Interferences in Atomic-Emission Spectrometry. Anal Chem. 1994; 66:A459–A467.

Buckley SG. Laser-Induced Breakdown Spectroscopy for Toxic Metal Emission Measurements: Experimental Considerations and Oxygen Quenching. Environ Eng Sci. 2005; 22:195–204.

Buckley SG, Johnsen HA, Hencken KR, Hahn DW. Implementation of Laser-Induced Breakdown Spectroscopy as a Continuous Emissions Monitor for Toxic Metals. Waste Manage. 2000; 20:455–462.

Canagaratna MR, Jayne JT, Jimenez JL, Allan JD, Alfarra MR, Zhang Q, Onasch TB, Drewnick F, Coe H, Middlebrook A, Delia A, Williams LR, Trimborn AM, Northway MJ, DeCarlo PF, Kolb CE, Davidovits P, Worsnop DR. Chemical and Microphysical Characterization of Ambient Aerosols with the Aerodyne Aerosol Mass Spectrometer. Mass Spectrom Rev. 2007; 26:185–222. [PubMed: 17230437]

Carranza JE, Fisher BT, Yoder GD, Hahn DW. On-Line Analysis of Ambient Air Aerosols Using Laser-Induced Breakdown Spectroscopy. Spectrochim Acta B-Atom Spectrosc. 2001; 56:851–864.

Carranza JE, Gibb E, Smith BW, Hahn DW, Winefordner JD. Comparison of Nonintensified and Intensified CCD Detectors for Laser-Induced Breakdown Spectroscopy. Appl Optics. 2003; 42:6016–6021.

Carranza JE, Hahn DW. Sampling Statistics and Considerations for Single-Shot Analysis Using Laser-Induced Breakdown Spectroscopy. Spectrochim Acta B-Atom Spectrosc. 2002; 57:779–790.

Author Manuscript Author Manuscript Author Manuscript Author Manuscript

Casini M, Harith MA, Palleschi V, Salvetti A, Singh DP, Vaselli M. Time-Resolved Libs Experiment for Quantitative-Determination of Pollutant Concentrations in Air. Laser Part Beams. 1991; 9:633–639.

Castle BC, Talabardon K, Smith BW, Winefordner JD. Variables Influencing the Precision Of Laser-Induced Breakdown Spectroscopy Measurements. Appl Spectrosc. 1998; 52:649–657.

Cheng MD. Real-Time Measurement of Trace Metals on Fine Particles by Laser-Induced Plasma Techniques. Fuel Process Technol. 2000; 65:219–229.

Cheng MD. Field Measurement Comparison of Aerosol Metals Using Aerosol Beam Focused Laser-Induced Plasma Spectrometer and Reference Methods. Talanta. 2003; 61:127–137. [PubMed: 18969171]

Chinni R, Cremers DA, Multari R. Analysis of Material Collected on Swipes using Laser-Induced Breakdown Spectroscopy. Appl Optics. 2010; 49:C143–C152.

Cremers DA, Archuleta FL, Martinez RJ. Evaluation of the Continuous Optical Discharge for Spectrochemical Analysis. Spectrochim Acta B-Atom Spectrosc. 1985; 40:665–679.

Cremers DA, Radziemski LJ. Direct Detection of Beryllium on Filters Using the Laser Spark. Appl Spectrosc. 1985; 39:57–63.

Cunat J, Fortes FJ, Laserna JJ. Real Time and in Situ Determination of Lead in Road Sediments using a Man-Portable Laser-Induced Breakdown Spectroscopy Analyzer. Anal Chim Acta. 2009; 633:38–42. [PubMed: 19110113]

Diwakar PK, Jackson PB, Hahn DW. The Effect of Multi-Component Aerosol Particles on Quantitative Laser-Induced Breakdown Spectroscopy: Consideration of Localized Matrix Effects. Spectrochim Acta B-Atom Spectrosc. 2007; 62:1466–1474.

Diwakar, PK.; Kulkarni, P.; Birch, ME. Matrix Effect in Substrate Based Laser-Induced Breakdown Spectroscopy. Proceedings of the 6th International Conference on Laser-Induced Breakdown Spectroscopy; September 13–17; Memphis, TN. 2010.

Diwakar, PK.; Kulkarni, P. Spark-Induced Breakdown Spectroscopy for Near Real Time Elemental Analysis of Aerosols. Proceedings of the 3rd North American Symposium on LIBS; July 18–20; Clearwater, FL. 2011.

Dixon PB, Hahn DW. Feasibility of Detection and Identification of Individual Bioaerosols Using Laser-Induced Breakdown Spectroscopy. Anal Chem. 2005; 77:631–638. [PubMed: 15649064]

Duan YX, Su YX, Jin Z, Abeln SP. A field Portable Plasma Source Monitor for Real-Time Air Particulate Monitoring. Anal Chem. 2000; 72:1672–1679. [PubMed: 10763268]

Fink H, Panne U, Niessner R. Process Analysis of Recycled Thermoplasts from Consumer Electronics by Laser-Induced Plasma Spectroscopy. Anal Chem. 2002; 74:4334–4342. [PubMed: 12236340]

Fisher BT, Johnsen HA, Buckley SG, Hahn DW. Temporal Gating for the Optimization of Laser-Induced Breakdown Spectroscopy Detection and Analysis of Toxic Metals. Appl Spectrosc. 2001; 55:1312–1319.

Flagan, RC.; Seinfeld, JH. Fundamentals of Air Pollution Engineering. Prentice Hall, Inc.; Upper Saddle River, NJ: 1988.

Flower WL, Peng LW, Bonin MP, French NB, Johnsen HA, Ottesen DK, Renzi RF, Westbrook LV. A Laser-Based Technique to Continuously Monitor Metal Aerosol Emissions. Fuel Process Technol. 1994; 39:277–284.

Gaft M, Sapir-Sofer I, Modiano H, Stana R. Laser Induced Breakdown Spectroscopy for Bulk Minerals Online Analyses. Spectrochim Acta B-Atom Spectrosc. 2007; 62:1496–1503.

Gaudiuso R, Dell'Aglio M, De Pascale O, Senesi GS, De Giacomo A. Laser Induced Breakdown Spectroscopy for Elemental Analysis in Environmental, Cultural Heritage and Space Applications: A Review of Methods and Results. Sensors. 2010; 10:7434–7468. [PubMed: 22163611]

Gornushkin IB, Anzano JM, King LA, Smith BW, Omenetto N, Winefordner JD. Curve of Growth Methodology Applied to Laser-Induced Plasma Emission Spectroscopy. Spectrochim Acta B-Atom Spectrosc. 1999; 54:491–503.

Gornushkin IB, Amponsah-Manager K, Smith BW, Omenetto N, Winefordner JD. Microchip Laser-Induced Breakdown Spectroscopy: A Preliminary Feasibility Investigation. Appl Spectrosc. 2004; 58:762–769. [PubMed: 15282039]

Author Manuscript Author Manuscript Author Manuscript Author Manuscript

Gottfried JL, De Lucia FC, Munson CA, Miziolek AW. Standoff Detection of Chemical and Biological Threats Using Laser-Induced Breakdown Spectroscopy. Appl Spectrosc. 2008; 62:353–363. [PubMed: 18416891]

Goujon J, Giakoumaki A, Pinon V, Musset O, Anglos D, Georgiou E, Boquillon JP. A Compact and Portable Laser-Induced Breakdown Spectroscopy Instrument for Single and Double Pulse Applications. Spectrochim Acta B-Atom Spectrosc. 2008; 63:1091–1096.

Gronlund R, Lundqvist M, Svanberg S. Remote Imaging Laser-Induced Breakdown Spectroscopy and Remote Cultural Heritage Ablative Cleaning. Opt Lett. 2005; 30:2882–2884. [PubMed: 16279457]

Hahn DW, Flower WL, Hencken KR. Discrete Particle Detection and Metal Emissions Monitoring Using Laser-Induced Breakdown Spectroscopy. Appl Spectrosc. 1997; 51:1836–1844.

Hahn DW. Laser-Induced Breakdown Spectroscopy for Sizing and Elemental Analysis of Discrete Aerosol Particles. Appl Phys Lett. 1998; 72:2960–2962.

Hahn DW, Lunden MM. Detection and Analysis of Aerosol Particles by Laser-Induced Breakdown Spectroscopy. Aerosol Sci Tech. 2000; 33:30–48.

Hao LQ, Wang ZY, Huang MQ, Fang L, Zhang WJ. Real-Time Measurements of Chemical Compositions of Secondary Organic Aerosol and Analysis of Reaction Mechanisms Using Single Aerosol Laser Mass Spectrometer. Int J Environ Pollut. 2009; 39:168–186.

Hohreiter V, Hahn DW. Calibration Effects for Laser-Induced Breakdown Spectroscopy of Gaseous Sample Streams: Analyte Response of Gas-Phase Species Versus Solid-Phase Species. Anal Chem. 2005; 77:1118–1124. [PubMed: 15858994]

Hrdlicka A, Prokes L, Stankova A, Novotny K, Vitesnikova A, Kanicky V, Otruba V, Kaiser J, Novotny J, Malina R, Palenikova K. Development of a Remote Laser-Induced Breakdown Spectroscopy System for Investigation of Calcified Tissue Samples. Appl Optics. 2010; 49:C16–C20.

Huang SH, Chen CC. Loading Characteristics of a Miniature Wire-Plate Electrostatic Precipitator. Aerosol Sci Tech. 2003; 37:109–121.

Hutchinson, IH. Principles of Plasma Diagnostics. 2nd. Cambridge University Press; Cambridge: 2002.

Ingley, JD.; Crouch, SR. Spectrochemical Analysis. Prentice Hall Inc.; Upper Saddle River, NJ: 1988. p. 174

Kanazawa S, Ohkubo T, Nomoto Y, Adachi T, Chang JS. Simultaneous Measurements of Wire Electrode Surface Contamination and Corona Discharge Characteristics in an Air-Cleaning Electrostatic Precipitator. IEEE Trans Ind Appl. 1997; 33:279–285.

Kuhlen T, Frickee-Begemann C, Strauss N, Noll R. Analysis of Size-Classified Fine and Ultrafine Particulate Matter on Substrates with Laser-Induced Breakdown Spectroscopy. Spectrochim Acta B-Atom Spectrosc. 2008; 63:1171–1176.

Kulkarni, P.; Sorensen, CM.; Baron, PA.; Harper, M. Nonspherical Particle Measurements: Shape Factor, Fractals, and Fibers. In: Kulkarni, PS.; Baron, PA.; Willekwe, K., editors. Aerosol Measurement. Wiley; New York: 2011. Chapter 23

Lanza NL, Wiens RC, Clegg SM, Ollila AM, Humphries SD, Newsom HE, Barefield JE, Team C. Calibrating the ChemCam Laser-Induced Breakdown Spectroscopy Instrument for Carbonate Minerals on Mars. Appl Optics. 2010; 49:C211–C217.

Leone N, Fath G, Adam P. Advances in the Detection of Chemical and Biological Aerosolized Pollutants by Means of a Field-Transportable Laser-Induced Breakdown Spectroscopy-Based Detector. High Temp Mater Process. 2007; 11:125–147.

Lin ZX, Chang L, Li J, Liu LM. Determination of As in Industrial Wastewater by Laser-Induced Breakdown Spectroscopy. Spectrosc Spect Anal. 2009; 29:1675–1677.

Lithgow GA, Robinson AL, Buckley SG. Ambient Measurements of Metal-Containing PM2.5 in an Urban Environment using Laser-Induced Breakdown Spectroscopy. Atmos Environ. 2004; 38:3319–3328.

Lithgow GA, Buckley SG. Effects of Focal Volume and Spatial Inhomogeneity on Uncertainty in Single-Aerosol Laser-Induced Breakdown Spectroscopy Measurements. Appl Phys Lett. 2005; 87:011501-1–011501-3.

Author Manuscript Author Manuscript Author Manuscript Author Manuscript

Mcdonald JR, Sparks LE. An Approach for Describing Electrical Characteristics of Precipitated Dust Layers. Japca J Air Waste Manage. 1980; 30:372–376.

Meissner K, Lippert T, Wokaun A, Guenther D. Analysis of Trace Metals in Comparison of Laser-Induced Breakdown Spectroscopy with LA-ICP-MS. Thin Solid Films. 2004; 453–454:316–322.

Myers RA, Karger AM, Hahn DW. Geiger Photodiode Array for Compact, Lightweight Laser-Induced Breakdown Spectroscopy Instrumentation. Appl Optics. 2003; 42:6072–6077.

Noll R, Bette H, Brysch A, Kraushaar M, Monch I, Peter L, Sturm V. Laser-Induced Breakdown Spectrometry—Applications for Production Control and Quality Assurance in the Steel Industry. Spectrochim Acta B-Atom Spectrosc. 2001; 56:637–649.

Noll R, Sturm V, Aydin U, Eilers D, Gehlen C, Hohne M, Lamott A, Makowe J, Vrenegor J. Laser-Induced Breakdown Spectroscopy-From Research to Industry, New Frontiers for Process Control. Spectrochim Acta B-Atom Spectrosc. 2008; 63:1159–1166.

Panne U, Neuhauser RE, Theisen M, Fink H, Niessner R. Analysis of Heavy Metal Aerosols on Filters by Laser-Induced Plasma Spectroscopy. Spectrochim Acta B-Atom Spectrosc. 2001; 56:839–850.

Panne U, Neuhauser RE, Haisch C, Fink H, Niessner R. Remote Analysis of a Mineral Melt by Laser-Induced Plasma Spectroscopy. Appl Spectrosc. 2002; 56:375–380.

Park K, Cho G, Kwak JH. Development of an Aerosol Focusing-Laser Induced Breakdown Spectroscopy (Aerosol Focusing-LIBS) for Determination of Fine and Ultrafine Metal Aerosols. Aerosol Sci Tech. 2009; 43:375–386.

Pierce, W.; Christian, SM.; Myers, MJ.; Myers, JD. Field-Testing for Environmental Pollutants Using Briefcase Sized Portable LIBS System. Proceedings of the 3rd International Conference on Laser Induced Plasma Spectroscopy and Applications; 28 September–1 October; Malaga, Spain. 2004.

Pope CA, Burnett RT, Thun MJ, Calle EE, Krewski D, Ito K, Thurston GD. Lung Cancer, Cardiopulmonary Mortality, and Long-Term Exposure to Fine Particulate Air Pollution. J Am Med Assoc. 2002; 287:1132–1141.

Salle B, Cremers DA, Maurice S, Wiens RC, Fichet P. Evaluation of a Compact Spectrograph for In-Situ and Stand-Off Laser-Induced Breakdown Spectroscopy Analyses of Geological Samples on Mars Missions. Spectrochim Acta B-Atom Spectrosc. 2005; 60:805–815.

Singh JP, Yueh FY, Zhang HS, Cook RL. Study of Laser Induced Breakdown Spectroscopy as a Process Monitor and Control Tool for Hazardous Waste Remediation. Process Control Qual. 1997; 10:247–258.

Wang Z, King SM, Freney E, Rosenoern T, Smith ML, Chen Q, Kuwata M, Lewis ER, Poschl U, Wang W, Buseck PR, Martin ST. The Dynamic Shape Factor of Sodium Chloride Nanoparticles as Regulated by Drying Rate. Aerosol Sci Tech. 2010; 44:939–953.

Wexler, AS.; Murray, VJ. Real Time Particle Analysis by Mass Spectrometry. In: Kulkarni, PS.; Baron, PA.; Willekwe, K., editors. Aerosol Measurement. Wiley; New York: 2011. Chapter 11

White HJ. Resistivity Problem in Electrostatic Precipitation. J Air Pollut Control Assoc. 1974; 24:313–338.

Young RP, Dubard JL, Sparks LE. The Onset of Electrical Breakdown in Dust Layers. 2. Effective Dielectric-Constant and Local Field Enhancement. JAPCA. 1988; 38:1518–1522.

Zelenyuk A, Imre D. Beyond Single Particle Mass Spectrometry: Multidimensional Characterisation of Individual Aerosol Particles. Int Rev Phys Chem. 2009; 28:309–358.

Zhuang Y, Kim YJ, Lee TG, Biswas P. Experimental and Theoretical Studies of Ultra-Fine Particle Behavior in Electrostatic Precipitators. J Electrostat. 2000; 48:245–260.

Author Manuscript Author Manuscript Author Manuscript Author Manuscript

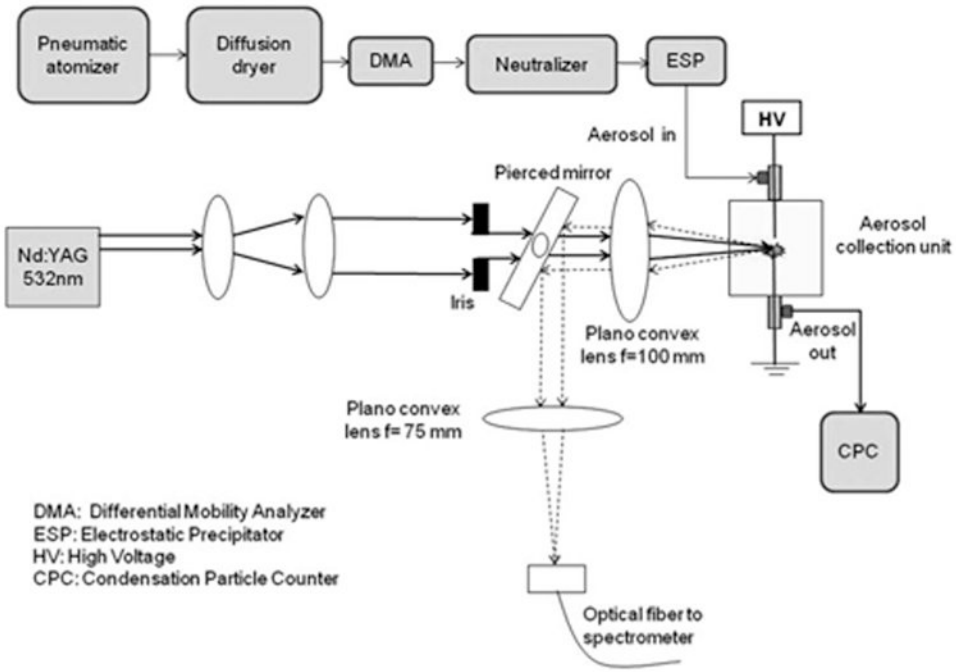

Fig. 1.
Schematic diagram of the experimental setup used in this work.

Author Manuscript Author Manuscript Author Manuscript Author Manuscript

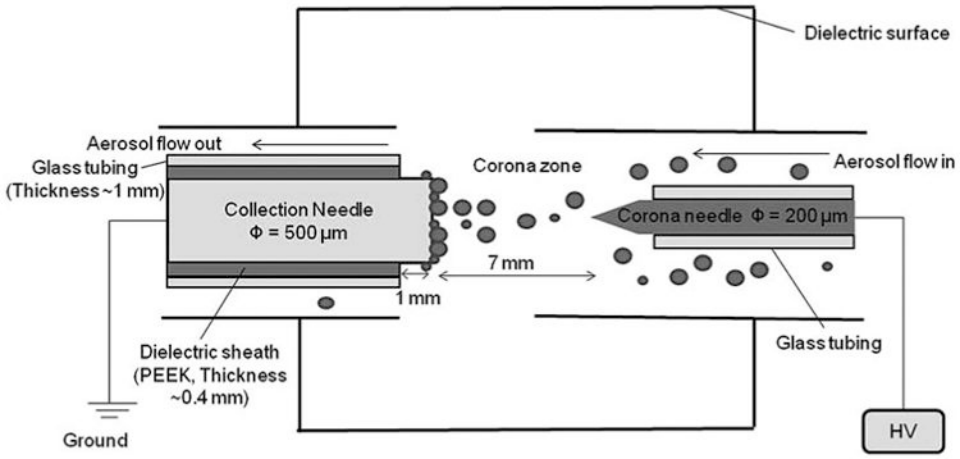

Fig. 2.

Microneedle electrode assembly designed to charge and collect particles for subsequent analysis by LIBS (not to scale).

Author Manuscript Author Manuscript Author Manuscript Author Manuscript

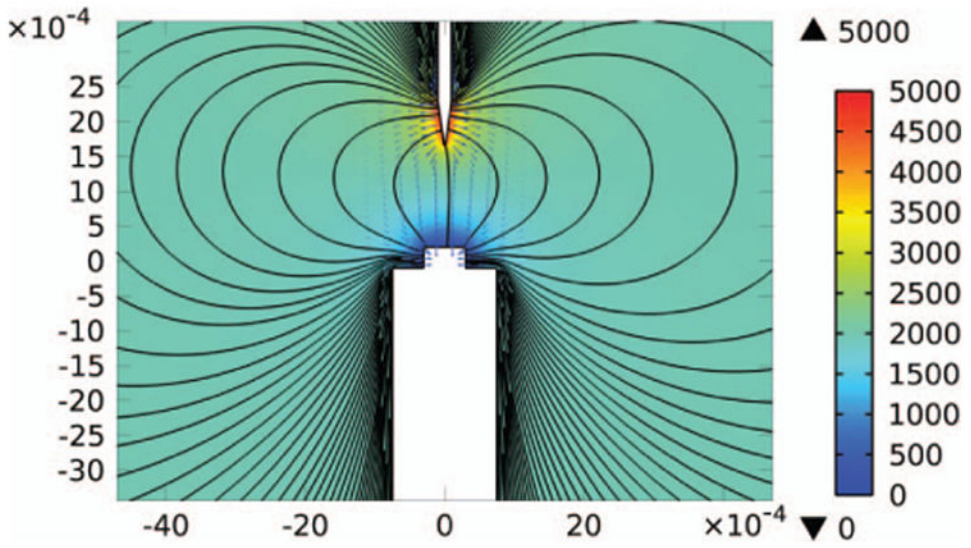

Fig. 3.

Distribution of electric potential and electric field strength around the corona and collection needle. *x*- and *y*-axes show distance in meters. Grayscale contour shows distribution of potential (in V) when 5000 V is applied on the corona needle and the collection needle is grounded. Electric field streamlines are also shown. The arrows indicate direction of electric field, with their length proportional to the strength of the field. Presence of corona was neglected in the simulation. (Color figure available online.)

Author Manuscript Author Manuscript Author Manuscript Author Manuscript

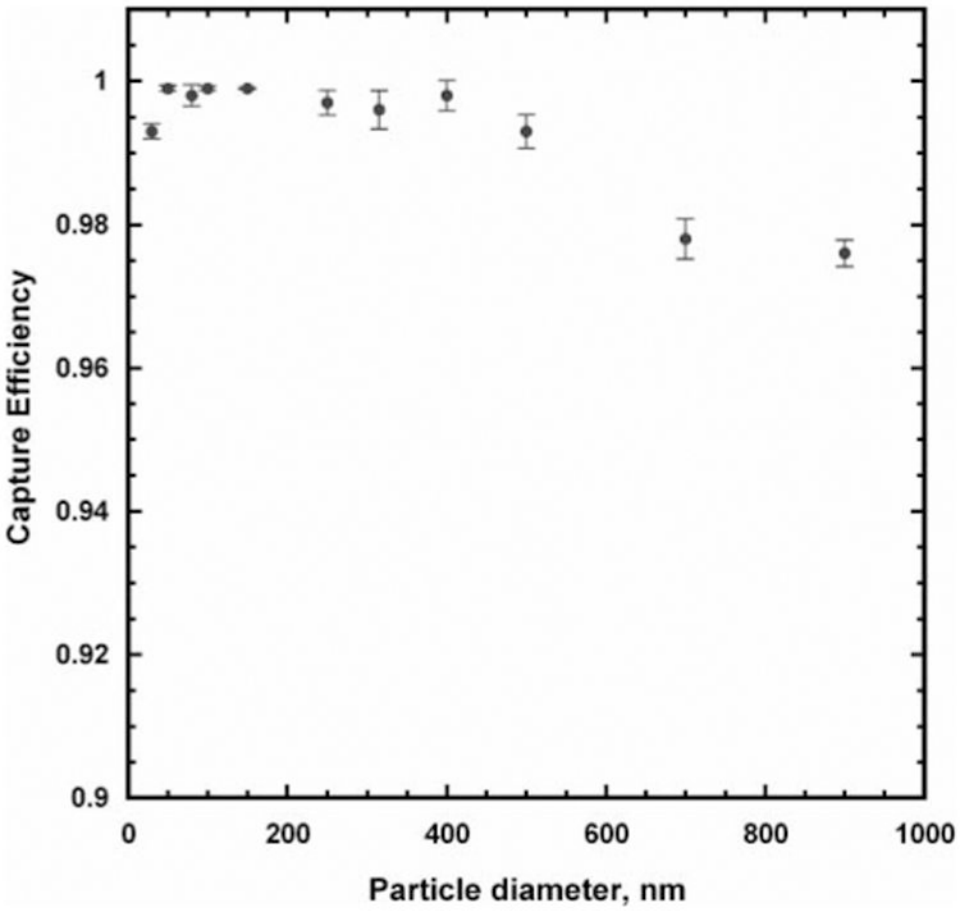

Fig.4.

Capture efficiency of collection electrode for various particle diameters in the submicrometer size range. Error bars represent ± standard deviation over four different measurements.

Author Manuscript Author Manuscript Author Manuscript Author Manuscript

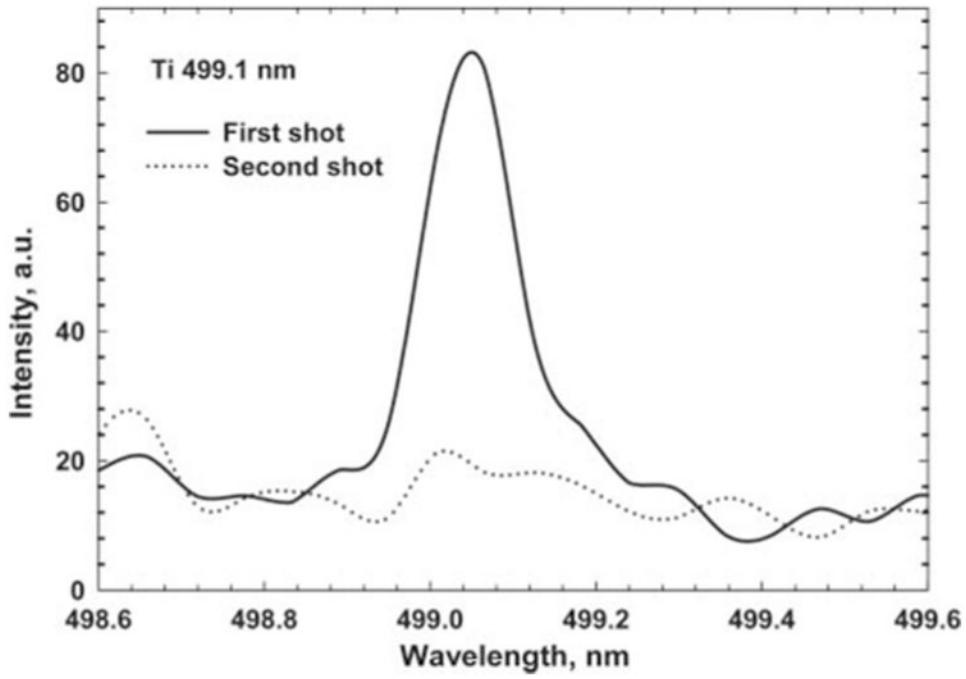

Fig. 5.
LIBS signal for deposited Ti aerosol from the first and second laser shot.

Author Manuscript Author Manuscript Author Manuscript Author Manuscript

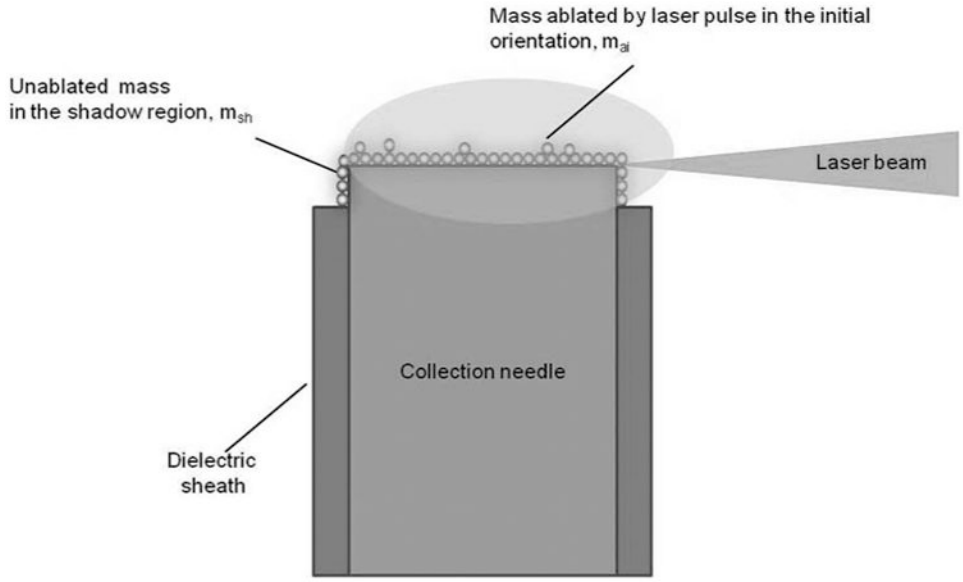

Fig. 6.

Schematic diagram showing orientation of the needle with respect to laser beam and shadow region.

Author Manuscript Author Manuscript Author Manuscript Author Manuscript

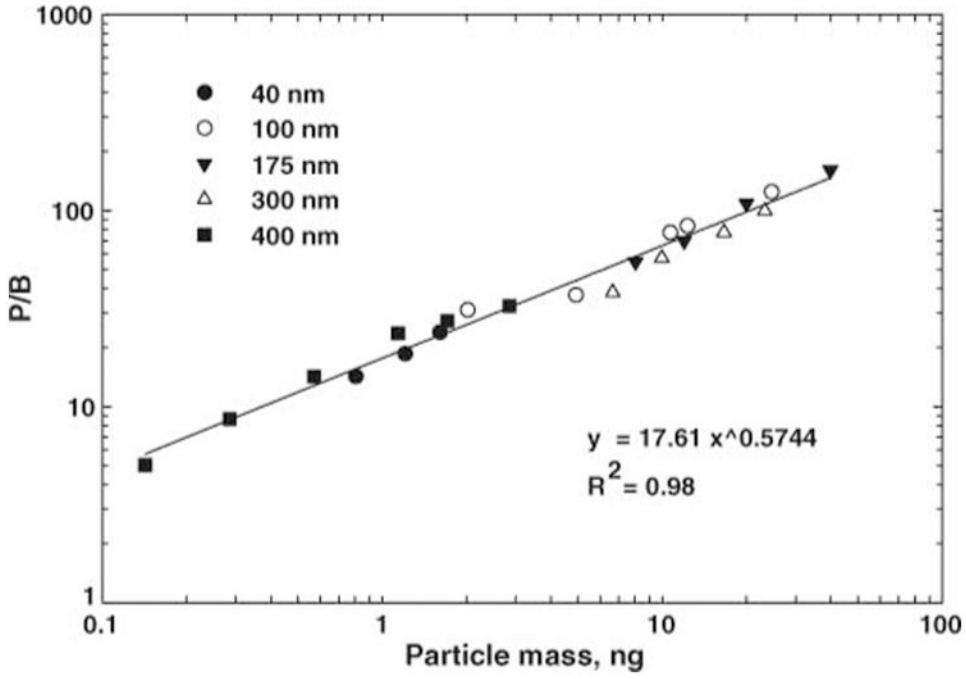

Fig. 7.
Na calibration curve constructed from particle sizes varying from 40 to 400 nm.

Author Manuscript Author Manuscript Author Manuscript Author Manuscript

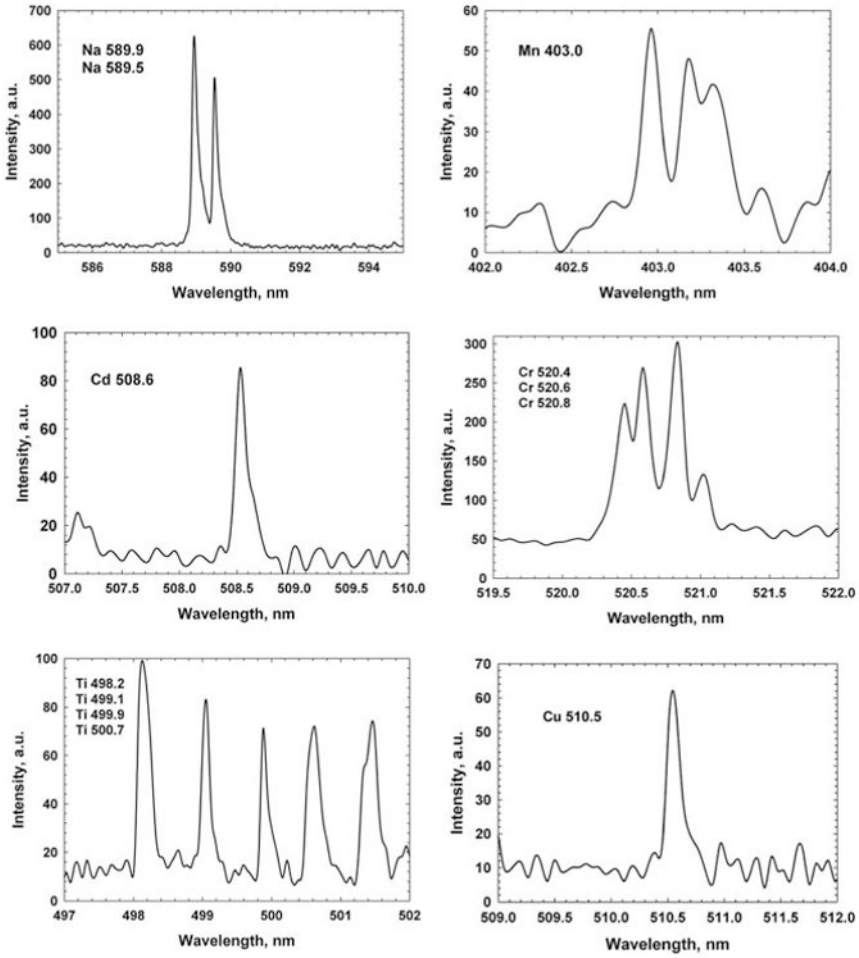

Fig. 8.

Representative LIBS spectra for Cd, Cr, Cu, Mn, Na, and Ti. Wavelengths of the peaks listed in upper left-hand corner are in nanometers.

Author Manuscript Author Manuscript Author Manuscript Author Manuscript

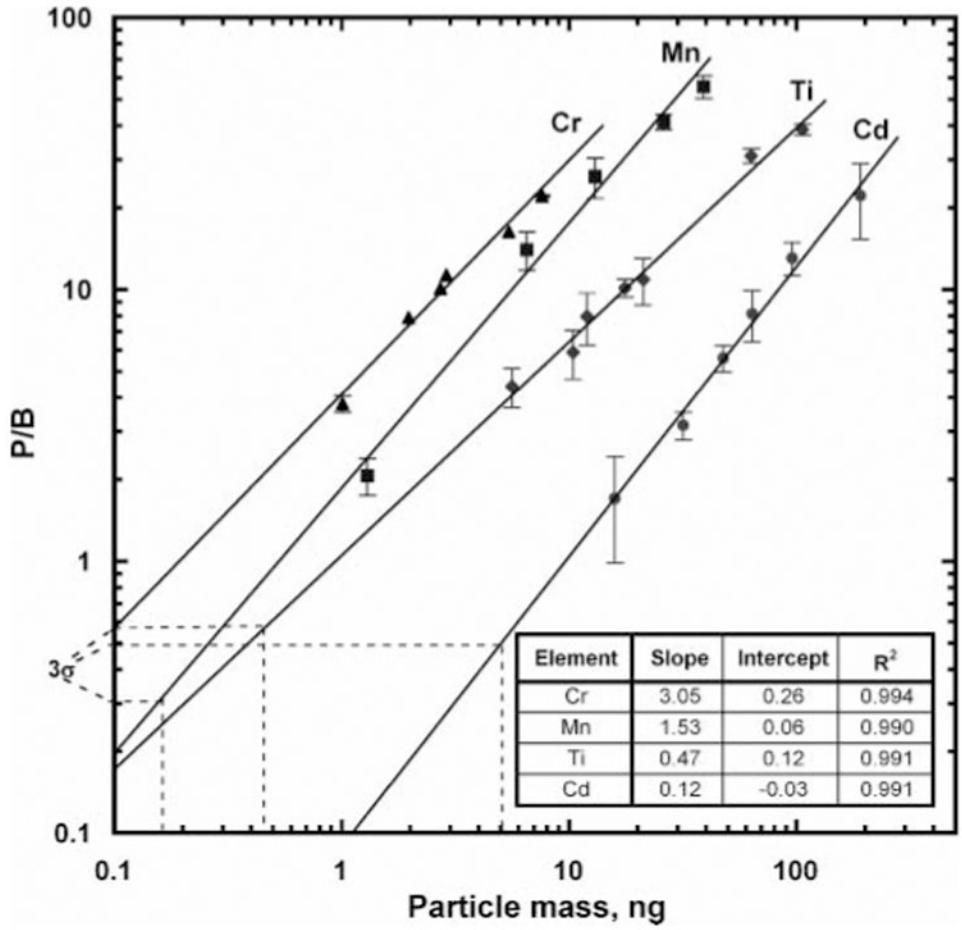

Fig. 9.

Representative calibration curves for Cr, Cd, Mn, and Ti. Cd, Cr, and Mn calibration curves were obtained using 50 nm particles. Ti calibration curve was obtained using 50 and 80 nm particles. Error bars represent ± standard deviation over five different repeat measurements. Slope, *y*-intercept, and R^2 value of a linear fit are also shown for each element. 3σ value for Mn, Ti, and Cd are shown as *y*-intercept in the plot.

Author Manuscript Author Manuscript Author Manuscript Author Manuscript

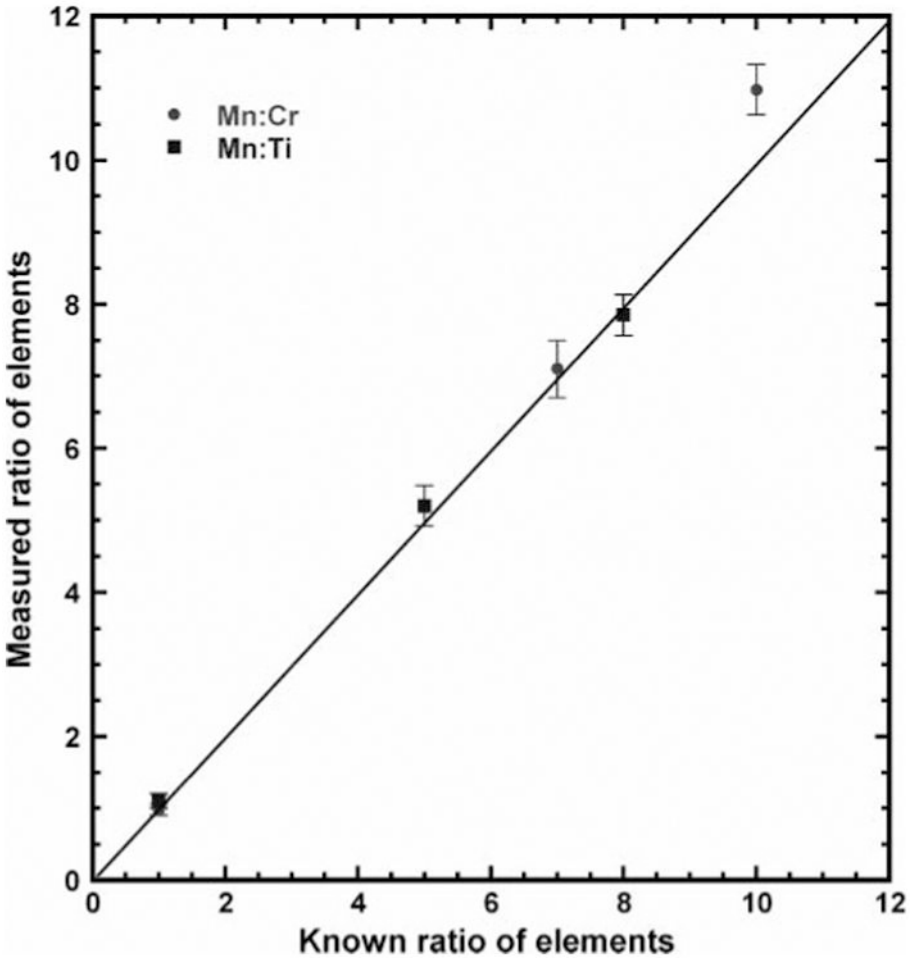

Fig. 10.
Comparison of known and measured ratios of elements in a test aerosol.

Author Manuscript Author Manuscript Author Manuscript Author Manuscript

Table 1

Description of test aerosol source and generation system used in this study

Element	Source	Chemical composition	Mass fraction	Density of salt (g/cm^3)	Aerosol generation method
Cd	Elemental standard solution (inorganic ventures)	Cadmium nitrate	0.47	3.6	Pneumatic atomizer
Cr	Elemental standard solution (Spex certiprep)	Chromium nitrate nonahydrate	0.13	1.85	Pneumatic atomizer
Cu	Elemental standard solution (inorganic ventures)	Copper nitrate	0.33	3.05	Pneumatic atomizer
Mn	Elemental standard solution (Spex certiprep)	Manganese nitrate	0.3	1.54	Pneumatic atomizer
Na	Sodium chloride solution	Sodium chloride	0.39	2.165	Pneumatic atomizer[a]
Ti	Elemental standard solution (Spex certiprep)	Ammonium hexafluoro titanate	0.27	6.67	Pneumatic atomizer

[a]To generate aerosol in the larger diameter range from 500 to 900 nm, condensation monodisperse aerosol generator (CMAG; model 3475, TSI Inc.) was used.

Author Manuscript

Author Manuscript

Author Manuscript

Author Manuscript

Table 2
Experimental parameters used in the LIBS system

Laser energy	20 mJ
Wavelength	532 nm
Laser spot size	560 μm
Spectrometer wavelength range	200–980 nm
Delay time	1.3 μs
Integration time	1 ms
Aerosol sample flow rate	1.5 L min^{-1}
Operating voltage for corona	5–5.6 kV
Distance between the needles	7 mm
Corona current	1 μA
Collecting needle tip diameter	500 μm

Author Manuscript

Author Manuscript

Author Manuscript

Author Manuscript

Table 3

Selected wavelength and corresponding energy level of elements for LIBS analysis

Element	Wavelength (nm)	Energy (cm^{-1})
Cd	508.58	31,826.95–51,483.98
Cu	510.55	11,202.57–30,783.69
Mn	403.07	0–24,802.25
Na	588.99	0–16,973.37
Cr	520.84	593.16–26,787.50
Ti	499.10	742.76–26,772.97

Author Manuscript

Author Manuscript

Author Manuscript

Author Manuscript

Table 4

Percentage mass fraction (m_{sh}/m_{ai}) present in the "shadow region" at different degrees of rotation of the collection electrode about the longitudinal axis[a]

Element	% (m_{sh}/m_{ai}) 90°	% (m_{sh}/m_{ai}) 180°	% (m_{sh}/m_{ai}) 270°	Total % (m_{sh}/m_{ai})
Cd	1.47 (0.14)*	10.29 (2.58)	2.72 (0.04)	14.49
Cu	1.13 (0.36)	8.96 (1.64)	2.8(1.25)	12.992
Mn	1.28 (0.02)	11.63 (0.65)	1.56 (0.13)	14.482

*Numbers in the parenthesis indicate standard deviation.

[a]The data were acquired using 50 nm particles for each element

Author Manuscript

Author Manuscript

Author Manuscript

Author Manuscript

Table 5

Overestimation of particle mass of nonspherical particles resulting from the simplifying assumption of spherical shape and mobility-equivalent size

Dynamic shape factor	% Mass overestimation
1.1	33.1
1.2	72.8
1.3	119.7
1.4	174.4
1.5	237.5

Author Manuscript Author Manuscript Author Manuscript Author Manuscript

Table 6

Comparison of mass detection limits of various elements with those from laboratory ICP-AES studies and other published studies

		LOD in terms of absolute mass (pg)					
Source	**Type of system**	**Cd**	**Cr**	**Cu**	**Mn**	**Na**	**Ti**
This work	SBC	5030	35	138	155	18	440
ICP-AES*	ICP-AES	129.5	53.65	296	17.5	7.3×10^4	212.75
Lithgow et al. 2004	FSA	–	0.17	0.015	0.176	–	–
Carranza et al. 2001	FSA	–	–	–	–	0.0033	–
Chinni et al. 2010	SWLIBS	9.7×10^5	5×10^5	296	17.5	–	–
Cremers et al. 1985	SBC	–	3500	870	–	5200	–

*ICP-AES detection limits were established using in-house laboratory bench-top system with sample flow rate of 0.001 L min^{-1} and total volume of the sample in the plasma to be 0.0925×10^{-3} L.

SWLIBS: Swipe LIBS.

Author Manuscript Author Manuscript Author Manuscript Author Manuscript

Table 7

Comparison of detection limits in terms of air concentration for various elements

		LOD in terms of air concentration ($\mu g/m^3$)					
Source	**Type of system**	**Cd**	**Cr**	**Cu**	**Mn**	**Na**	**Ti**
This work*	SBC	0.67	0.047	0.018	0.02	0.024	0.059
Fisher et al. 2001	FSA	60	30	–	–	–	–
Cheng 2000	SPB	–	0.08	–	–	–	–
Amodeo et al. 2009	FSA	–	–	80	–	2	430
Duan et al. 2000	FSA-MIPS	1.3	0.31	0.088	2.3	–	–
Panne et al. 2001	SBC	1.19	0.11	0.02	0.08	–	0.39
Park et al. 2009	SPB	–	–	0.08	–	–	–

*Detection limit in air concentration calculated by assuming a collection time of 5 min and flow rate of 1.5 L min^{-1}.

SWLIBS: Swipe LIBS; MIPS: Microwave plasma spectroscopy.

Author Manuscript

Author Manuscript

Author Manuscript

Author Manuscript

Table 8

LODs and associated uncertainties for various elements studied in this work

Element	LOD (ng)	Range of LOD (ng)*	% RSD of LOD
Cd	5.03	3.48–6.19	33
Cr	0.035	0.029–0.039	13
Cu	0.138	0.128–0.158	11
Mn	0.155	0.152–0.17	6
Na	0.018	0.014–0.025	4
Ti	0.44	0.26–0.5	21

*Range of LOD indicates minimum and maximum of LODs obtained in five individual sets of measurements.

Author Manuscript Author Manuscript Author Manuscript Author Manuscript

Table 9

Minimum collection time (in seconds) required to analyze polydisperse aerosols of various geometric mean diameters with N_t = 100 cm^{-3} and σ_g = 1.5 for various inorganic compounds

	Minimum collection time (s)					
Geometric mean diameter, d_{pg} (nm)	Cd (CdO)	Cr (Cr_2O_3)	Cu (CuO)	Mn ($MnCO_3$)	Na (NaCl)	Ti (TiO_2)
10	684782	14135	26934	10614	4425	21284
25	46292	955	1821	717	299	1439
50	5786	119	227	90	37	180
100	723	15	28	11	5	22
500	6	0.1	0.2	0.1	0.04	0.2

Aerosol Sci Technol. Author manuscript; available in PMC 2015 December 11.